

Modeling the Thermal Conductivity of Porous Electrodes of Li-Ion Batteries as a Function of Microstructure Parameters

Dieter Oehler,* Philipp Seegert, and Thomas Wetzel

The performance and lifetime of lithium-ion batteries are strongly influenced by the temperature distribution within the cells, as electrochemical reactions, transport properties, and aging effects are temperature dependent. However, thermal analysis and numerical simulation of the temperature inside the cells can only be as accurate as the underlying data on thermal transport properties. This contribution presents a numerical and analytical model for predicting the thermal conductivity of porous electrodes as a function of microstructure parameters. Both models account for the morphology of the electrode structures and bulk material properties of the constitutive components. Structural parameters considered in both models alike are the porosity of the electrode coatings, particle size distribution, particle shape, particle contact areas, and binder carbon black distribution. The numerical model is based on the well-established finite volume discretization, allowing for detailed 3D analyses. The analytical model is an extension of the well-known Zehner–Bauer–Schluender approach for solid packing and provides fast predictions of the effects of parameter variations. The results of both models have been successfully verified against each other and compared to literature data and experimental measurements.

1. Introduction


The microstructure and composition of the porous electrodes of lithium-ion batteries have a strong influence on their resulting effective thermal conductivity, as has been shown by Maleki et al., Sangrós et al., and Vadakkepatt et al. in their publications.^[1–3] Chen et al., Samba et al., Guo et al., and Jeon et al. discuss the strong influence of thermal transport properties, i.e., thermal conductivity, density, and specific heat capacity during the cell operation and their effects on the electrochemical–

thermal behavior.^[4–7] Numerous publications, such as Schuster et al., Ramadass et al., Zhang et al., and Fleckenstein et al. describe the dependence of aging mechanisms on elevated temperature levels and nonuniform temperature distributions within the cell.^[8–12] Thermal management systems are used to avoid critical temperature levels. However, as heat transport by conduction relies physically on temperature gradients, whether thermal management systems contribute to reducing temperature gradients or if they are even increased in certain operation conditions depend on their suitable design. This effect is becoming more critical with increasing cell dimensions, leading to longer thermal transport paths. Yang et al.^[13] described that well-designed thermal management systems help to increase performance and, according to Werner et al.,^[14,15] also reduce the aging of the batteries. However, good design of thermal management systems, based on predictive

design tools, requires knowledge of the cell-specific thermal transport properties. However, there are not many sources, particularly for the effective thermal conductivity of the porous electrodes of the lithium-ion cells, nor are there established methods for its prediction. A few values according to Maleki et al., Chen et al., Sangrós et al., and Vadakkepatt et al.^[1–4] in the existing literature are used for electrochemical–thermal simulation, which do not usually contain information on microstructure parameters and composition, as can be seen in the publications by Chen et al., Samba et al., Guo et al., and Jeon et al.^[4–7] **Table 1** contains a detailed overview of the data sets available in the literature for the effective thermal conductivity of porous electrodes of lithium-ion battery cells.

The literature data in Table 1 vary between 0.32 and 3.5 W m^{−1} K^{−1} for the porous graphite coating of the anodes, depending on the measuring method and fluid within the pores during the measurement. Gases, such as helium, nitrogen, argon or carbon dioxide, are used for filling the pore space during measurement (as will be discussed in detail in Section 4) as electrolytes are extremely volatile and noncompatible with established measurement methods. The data for LiCoO₂ (LCO)-based cathode coatings vary in a range from 0.26 to 2.75 W m^{−1} K^{−1} and for nickel manganese cobalt oxide (NMC) between 0.2 and 0.9 W m^{−1} K^{−1}. According to Richter et al.,^[18] the lithium iron

D. Oehler, P. Seegert, Prof. T. Wetzel
Institute of Thermal Process Engineering (TVT)
Karlsruhe Institute of Technology (KIT)
Engelbert-Arnold-Str. 4, 76131 Karlsruhe, Germany
E-mail: dieter.oehler@kit.edu

 The ORCID identification number(s) for the author(s) of this article can be found under <https://doi.org/10.1002/ente.202000574>.

© 2020 The Authors. Published by Wiley-VCH GmbH. This is an open access article under the terms of the Creative Commons Attribution-NonCommercial-NoDerivs License, which permits use and distribution in any medium, provided the original work is properly cited, the use is non-commercial and no modifications or adaptations are made.

DOI: 10.1002/ente.202000574

Table 1. Comparison of data on thermal conductivity of porous electrode coatings of different cell chemistries and cell states published in literature. All values with no unit are given in $\text{W m}^{-1} \text{K}^{-1}$. The acronyms XALT, Hohsen, and MTI represent cell manufacturers.

Author	Chemistry	Anodes	Cathodes	Microstructure
Maleki et al. ^[16]	Graphite, LCO without electrolyte	0.89 (2.45 V) – 1.2 (3.75 V)	2.33 (2.45 V) – 2.49 (3.75 V)	Particle size: LCO (10–20 μm) Graphite (20–45 μm)
Chen et al. ^[4]	Graphite, LCO with electrolyte	1.04	1.58	Not specified
Gotcu et al. ^[17]	–; NMC N ₂ -atmosphere	–	0.45 (SOC 100%) 0.34 (SOC 0%)	Porosity: 40% (SOC 100%) Porosity: 45% (SOC 0%) Composition: 90 wt% NMC; 5 wt% PVDF; 5 wt% Carbon black
	–; LCO N ₂ -atmosphere	–	0.39 (SOC 100%) 0.29 (SOC 0%)	Porosity: 40% (SOC 100%) Porosity: 45% (SOC 0%) Composition: 90 wt% NMC; 5 wt% PVDF; 5 wt% Carbon black
Richter et al. ^[18]	XALT Graphite; NMC air-atmosphere	0.32 (2.3 bar) – 0.61 (11.5 bar)	0.30 (2.3 bar) – 0.39 (11.5 bar)	Not specified
	XALT Graphite; NMC with electrolyte	0.89 (2.3 bar) – 1.37 (11.5 bar)	0.82 (2.3 bar) – 0.90 (11.5 bar)	Not specified
	Hohsen Graphite; LCO air-atmosphere	0.26 (2.3 bar) – 0.52 (11.5 bar)	0.17 (2.3 bar) – 0.26 (11.5 bar)	Not specified
	Hohsen Graphite; LCO with electrolyte	1.11 (2.3 bar) – 1.38 (11.5 bar)	1.03 (2.3 bar) – 1.48 (11.5 bar)	Not specified
	MTI –; LFP air-atmosphere	–	0.13 (2.3 bar) – 0.15 (11.5 bar)	Not specified
	MTI –; LFP with electrolyte	–	0.32 (2.3 bar) – 0.36 (11.5 bar)	Not specified
Loges et al. ^[19]	Cell A Graphite; LCO CO ₂ -atmosphere	2.5 (5 °C) – 1.8 (45 °C)	2.0 (5 °C) – 0.7 (45 °C)	Porosity: 46% (SOC 0%) Porosity: 24% (SOC 0%)
	Cell B Graphite; LCO CO ₂ -atmosphere	2.75 (5 °C) – 2.00 (45 °C)	1.8 (5 °C) – 0.5 (45 °C)	Porosity: 47% (SOC 0%) Porosity: 29% (SOC 0%)
	Cell C Graphite; NMC CO ₂ -atmosphere	3.5 (5 °C) – 2.9 (45 °C)	0.25 (5 °C) – 0.20 (45 °C)	Porosity: 53% (SOC 0%) Porosity: 37% (SOC 0%)

phosphate (LFP)-based coatings have a range of 0.13 to $0.36 \text{ W m}^{-1} \text{K}^{-1}$. The data from Maleki et al. and Gotcu et al.,^[16,17] are based on the laser flash method. Here, the energy pulse of a xenon flash heats the bottom of the sample, while the time series of the temperature on the top is detected by an infrared sensor, as can be seen by Maleki et al. and Parker et al.^[16,20] The temporal development of this top-side temperature contains information on the thermal diffusivity that can be retracted by different methods, according to Parker et al., Cape et al., and McMasters et al.^[20–22] Gotcu et al. shows that the thermal diffusivity can then be used to calculate the thermal conductivity if the density and heat capacity of the sample are known.^[17] Photothermal deflection spectroscopy is described by Loges et al., Salazar et al., and Bertolotti et al.^[19,23–25] as a method

for the determination of the thermal diffusivity. Here, the sample is excited with a power-modulated laser, which leads to temperature oscillations. This creates an oscillating temperature gradient in the sample and the surrounding medium, which, in turn, causes gradients in the refractory index, a so-called thermal lens, in the surrounding medium.^[19,23–25] A detection laser is used to measure the fluctuating extension of the thermal lens. The thermal diffusivity of the porous coating can be determined by evaluating the deflection of the laser beam with a variety of evaluation schemes.^[19,23–25] The values from Richter et al. are based on the constant heat-flux method, in which steel cylinders are pressed onto the sample at a defined pressure.^[18] The temperature is controlled in such a way that a certain heat flux is transported through the sample. The thermal conductivity can be determined

from the heat flux and the temperature difference using Fourier's law. Burheim et al. shows that the method allows for a variation of contact pressures.^[26] While elevated contact pressure leads to a minimization of the contact resistance between the sample and cylinders, it may also cause an undefined disturbance of the microstructure of the sample, specifically lowering porosity, increasing particle–particle contact areas, typically being reflected in an increase of the thermal conductivity with increasing pressure.

Chen et al.^[4] and Richter et al.^[18] report thermal conductivity values for electrolyte-filled pore space, Richter et al.^[18] even in direct comparison to a coating filled with non-electrolyte. The sharp increase in thermal conductivity in the case of electrolytes compared with the ambient air-filled coating can be explained by the fact that this leads to a reduction in the thermal resistance between the steel cylinders and the sample. This is reflected in the increase in the thermal conductivity of $0.26 \text{ W m}^{-1} \text{ K}^{-1}$ for the medium air to $1.11 \text{ W m}^{-1} \text{ K}^{-1}$ for the electrolyte, regarding the Hohsen coating (see Richter et al.^[18] in Table 1). As a comparison, pure electrolyte has a thermal conductivity of 0.18 ^[27] to $0.45 \text{ W m}^{-1} \text{ K}^{-1}$ ^[4] and, therefore, a higher thermal conductivity than ambient air ($0.026 \text{ W m}^{-1} \text{ K}^{-1}$ ^[28]). The measuring results from Richter et al.^[18] suggest that the fluid and the thermal contact resistances have a great influence on the effective thermal conductivity. Therefore, precise numerical and experimental methods are needed to describe the influence of the filling fluid and electrolyte.

Table 1 also shows that the microstructure parameters and material composition are only partially specified. However, they have a strong influence on the thermal conductivity of porous electrodes. This is probably an additional reason for the scattering values of the effective thermal conductivity, in addition to the points discussed earlier.

The variations in effective thermal conductivity represented in Table 1, along with the vast variety of parameters and their wide ranges, make identifying representative values difficult and predicting cell- or coating-specific values practically impossible. Filling this gap experimentally is very expensive and bears strong uncertainties imposed by determining the numerous parameters. Therefore, several analytical and numerical approaches have been developed to describe the effective thermal conductivity of the porous electrodes. Sangrós et al.^[2] determined the effective thermal conductivity using the discrete element method. They consider the heat conduction through the active material (AM) phase, while neglecting the heat conduction through the binder carbon black (BCB) and electrolyte phase. He et al.^[29] reconstruct a porous anode coating using an approach they call the simulated-annealing method. The thermal simulation is done using the Lattice–Boltzmann method. The AM phase, binder and electrolyte phase are considered. He et al.^[29] have erroneously assumed a value of $1.04 \text{ W m}^{-1} \text{ K}^{-1}$ for the bulk thermal conductivity of the AM graphite, instead of the usual value of $140 \text{ W m}^{-1} \text{ K}^{-1}$, according to Sangrós et al.^[2] and Buerschaper.^[30] In addition, the carbon black (CB) content in the binder phase is also neglected. Vadakkepatt et al.^[3] use X-ray tomography or a dual-beam focused ion beam–scanning electron microscope for the reconstruction of real cathode coatings and calculate the thermal conductivity numerically using a volume-averaging technique. They consider the AM and the

electrolyte phase, and the BCB mixture as a homogeneous phase. In addition, Vadakkepatt et al.^[3] compare the numerical model with an enhanced analytical Bruggemann-type approach,^[31] where all phases are treated in a homogenized manner. It cannot, therefore, represent structural parameters other than porosity.

Two different predictive approaches are presented in this work that take a large set of microstructural parameters and bulk material properties of the electrode coating into consideration. The first one is a numerical model, based on a generic 3D geometry generation of the microstructure and solving the heat transport equation using the finite volume method. The second approach is an extension of the Zehner–Bauer–Schluender (ZBS) model,^[32–34] i.e., an analytical representation of the various complex thermal transport paths within the microstructure by a weighted combination of parallel and series connections of thermal resistances. The ZBS model was originally developed for the description of effective thermal transport within porous fillings, such as fixed beds. It has been extended in our work to represent the specific microstructure of porous electrode coatings, such as particle contact areas, particle distances, and the BCB phase and its distribution. A stochastic microstructure is generated by a newly developed structure-generation routine in the numerical model. Parameters, such as particle shape, porosity, BCB mixture and particle overlap, can be freely adjusted and applied to real microstructures. The BCB phase is modeled as so-called binder bridges, which form a binder network by overlapping. In contrast to the approaches presented so far in literature, the models in this contribution consider the morphology of the electrode structures and the bulk thermal conductivity of the individual material phases.

The article is organized in the following manner: Section 2 gives a description of the numerical model. In Section 2.1, the generation of the porous microstructure and the BCB network for the numerical model is presented. The generic microstructure geometries generated are compared with literature data on real electrode coatings. Section 2.2 briefly introduces the finite volume method as implemented in the open-source code OpenFOAM and the adaptation of it to the problem of heat conduction in porous electrode structures. The extension of the ZBS model is discussed in Section 3. Section 4 presents and discusses results of studies with varying values for porosity, electrode composition, and material properties. The numerical and analytical model are compared and verified regarding each other. The results of the models are also compared to existing literature data and our own measurements to check the validity for certain parameter sets. Section 5 provides a summary.

2. Numerical Simulation

2.1. Microstructure Generation

A structure generator developed in MATLAB in-house is used for the generation of a porous electrode structure, which stochastically deposits and sediments particles, one after the other, as graphic objects in a system volume of predefined size until a stable position of each particle is reached. The particle size distribution, particle shape (spheres, ellipsoids, super ellipsoids) and an initial rotation represent the input parameters.

An algorithm for the sedimentation of the particles in which a particle, starting from a random position, is lowered in a negative z-direction in a predetermined increment until it either reaches the lower system limitation or touches another, already positioned, particle and, ultimately, reaches a stable position. If the particle crosses one of the four lateral boundaries during the sedimentation process, the particle will be cut off, and on the opposite side, the cutout is created as a reflection. When a particle reaches the lower system limitation, which corresponds to the electrode current collector, it will be cut off by a user-defined length. This length is called a current collector cut and is used to adjust the contact area between the particles and the lower system limitation or current collector. A current collector cut of zero corresponds to a point contact of the particles and a value greater than zero corresponds to a cutting off of the particles, thus, creating a contact area between the AM phase and the current collector. The occurrence of collisions is checked during the sedimentation process after each lowering step using the Gilbert–Johnson–Keerthi algorithm according to Gilbert et al.^[35] When the sedimenting particle has reached a stable position, the next particle is generated at the upper system limitation and lowered downward. This is repeated until either the maximum particle number, previously calculated on the basis of the system volume and the average particle size of the specified particle size distribution, is reached or a particle protrudes beyond a predefined value above the upper system limitation, the so-called separator cut. Similar to the current collector cut, the contact area between the AM and the separator can be adjusted by the

separator cut. **Figure 1** shows an example of a generated structure of the system size $5 \times 5 \times 5 \mu\text{m}$ on the right-hand side. As shown in Figure 1, there is a current collector cut and a separator cut, so that the particles on the current collector or separator side have a contact area between the AM particles.

Information, such as the Cartesian coordinates of the particle centers and the particle size and shape, is automatically transferred to OpenSCAD, a code-based open-source computer-aided design (CAD) program. With this data, which is available in the MATLAB source code after the particle positioning, a SCAD file is created in OpenSCAD for each particle and each reflected particle. This SCAD file includes all the geometric information of the particles as string variables. The particle position, particle shape and, if necessary, a rotation is realized in the SCAD file code by the geometric operations translate, scale, and rotate. Due to the scale-operation and an implemented shrinkage factor, the particles can be shrunk or enlarged relative to their diameter to avoid or cause particle overlapping. If an overlap with another particle exists, an intersection process is started using the OpenSCAD Boolean operations, which removes the overlap volume from one particle and leaves the other one complete. Otherwise, the volume fraction would be calculated incorrectly (see **Figure 2**). After another check of the geometry in OpenSCAD, the final SCAD files of the particle are converted into stereolithography (STL) files. The STL files describe the surface of the particles using triangular facets and are needed for the meshing of the structure and the calculation of the volume fraction of the AM particles. If the volume fraction is higher

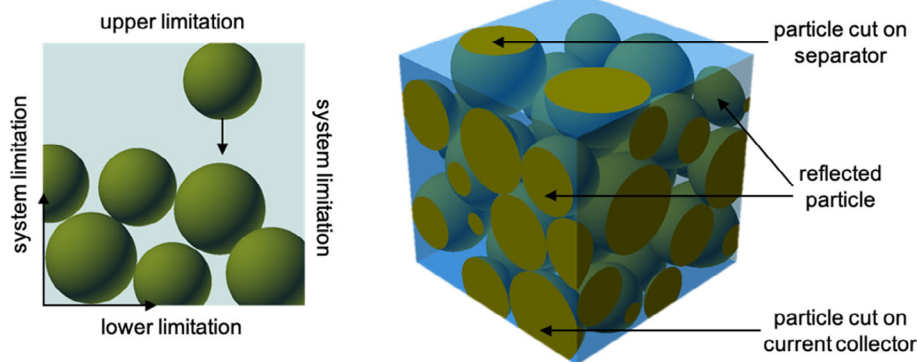


Figure 1. Left, schematic representation of the sedimentation process in the system volume. Right, representation of the current collector cut, a reflected particle, and the separator cut.

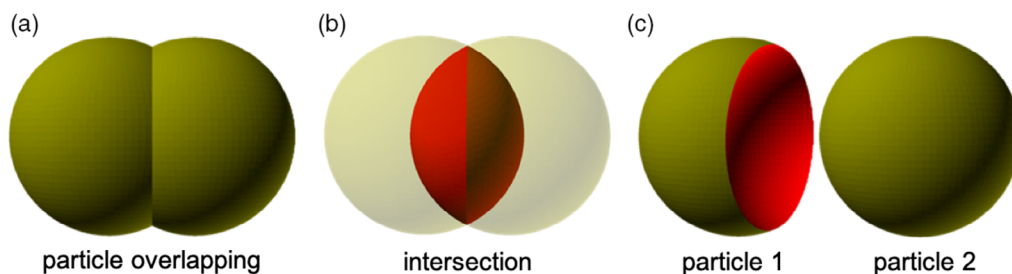


Figure 2. Stepwise generation of a particle overlap: a) particle overlapping, b) forming an intersection between the particles, c) resulting cut particle 1 and unchanged particle 2.

than the default value, particles are removed randomly from the structure until the fraction matches the desired amount within a defined tolerance.

Bauer et al.^[36] report in their article about the presence of BCB clusters. They also mentioned that the localization of the binder within the CB agglomerates is difficult to detect. Similar findings were reported by Almar et al.,^[37] whose contribution deals with the analysis of the microstructure by focused-ion beam tomography–scanning electron microscope images. They considered in their work the BCB mixture as a homogenized mixed phase. Pfaffmann et al.^[38] investigated the BCB distribution in porous electrodes with an energy selective backscattered detector. They showed that the binder seems to be mainly contained in the CB regions. As a conclusion, the BCB mixture is approximated as a homogeneous phase and in a next step inserted into the porous particle structure. Furthermore, the size of CB typically varies between 20 and 30 nm and thus shows a 100 to 200 times smaller particle size in comparison to the AM.^[37] The assumption of a homogeneous phase represents a simplified description of the BCB phase, for a reduction of computing time. The calculation of the effective thermal conductivities of the BCB mixture is explained in detail in Section 4. Rahani and Shenoy^[39] show two possible models of how the binder phase is distributed in a porous electrode structure: Binder shells and binder bridges. In the present structure-generation routine, this assumption is extended to the BCB mixture and therefore the homogeneous mixture is implemented in the form of binder shells and binder bridges. The user defines the amount of the BCB phase and the generation probability that a binder shell and/or bridge occurs on

a particle. In addition, a relative distance to the particle size for the generation of binder bridges must be specified. No more binder bridges occur above this maximum distance. The generation of the binder shells and bridges is carried out according to an iterative process in which, starting from a maximum value, the radius of the shell or bridge is reduced until the volume fraction desired is reached. The procedure for the creation of the binder shells and bridges is analogous to that of the particles. The MATLAB program uses string variables to generate the source code for the individual SCAD files for each binder object (shell or bridge). The binder for the shells is created as a sphere around the particles (see Figure 3a) and, in the next step, the actual particle is removed by the difference operation to create the binder shells (see Figure 3a,b). The cutting processes for each binder shell are again implemented in the individual existing SCAD file using string variables.

The individual steps for generating a binder bridge are shown in Figure 4. Firstly, a 2D polygon is created (see Figure 4a) based on the distance between two particles and their radii. In a next step, this polygon is transformed into a 3D rotational solid (see Figure 4b,c) using the OpenSCAD operation `rotate_extrude`. Finally, the OpenSCAD operation `difference` is used to cut off the overlap of the binder bridges with the particles (see Figure 4d).

Comparable to the particles, the binder objects must also be checked for possible overlaps with all other objects: Particles, reflections of particles, binder shells, reflections of binder shells, and binder bridges. Finally, an STL file is created for each binder object comparable to the particle phase. Figure 5 shows an example

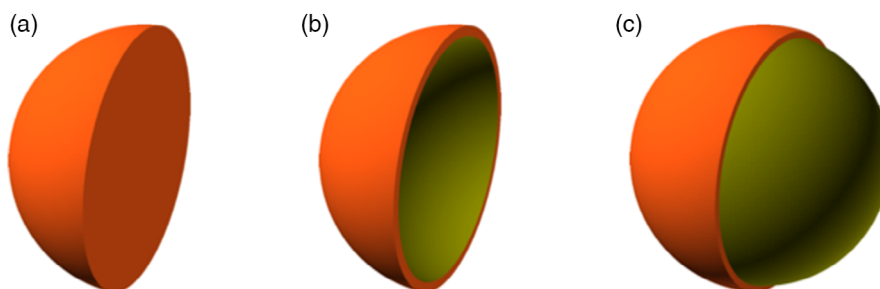


Figure 3. Stepwise generation of a binder shell: a) generation of a binder sphere, b,c) resulting binder shell after cutting process with particle.

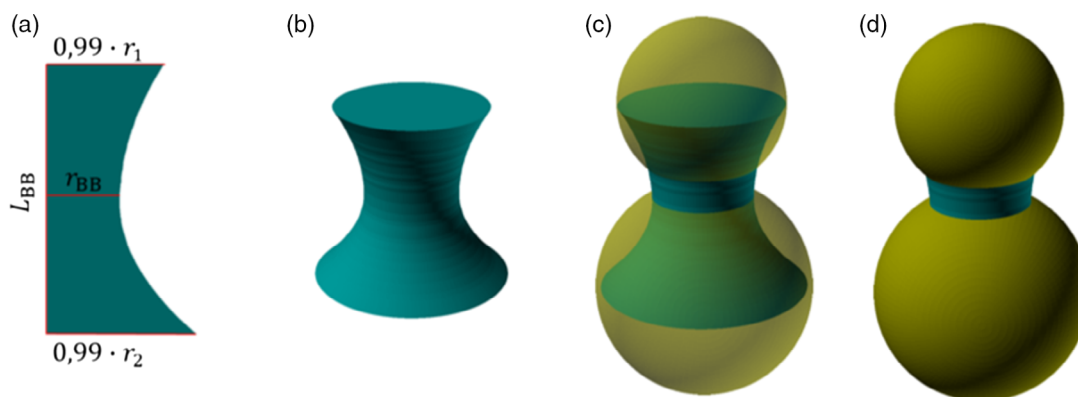


Figure 4. Stepwise generation of a binder bridge: a) 2D polygon with constriction, b) binder bridge as 3D body of rotation, c) positioning of the binder bridge between particles, and d) binder bridge after cutting process with particles.

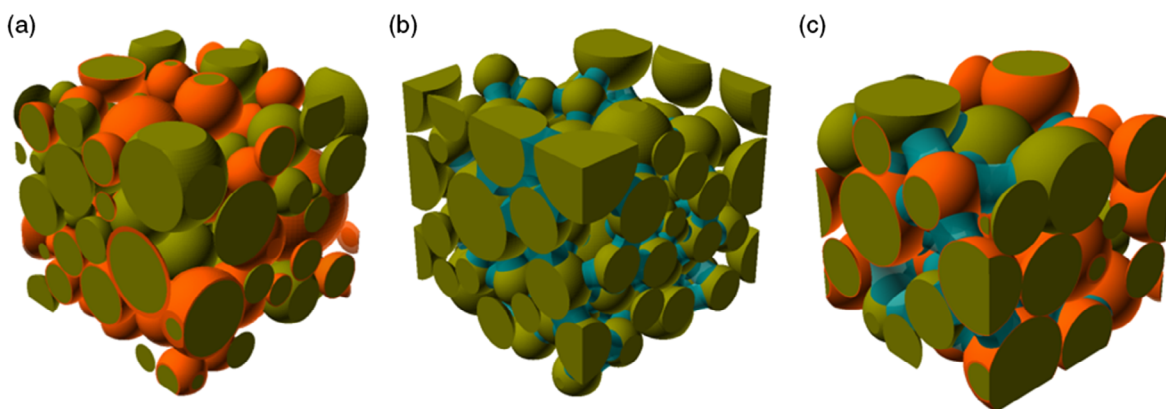


Figure 5. a) A structure with binder shells, b) structure with binder bridges, and c) structure with binder shells and binder bridges.

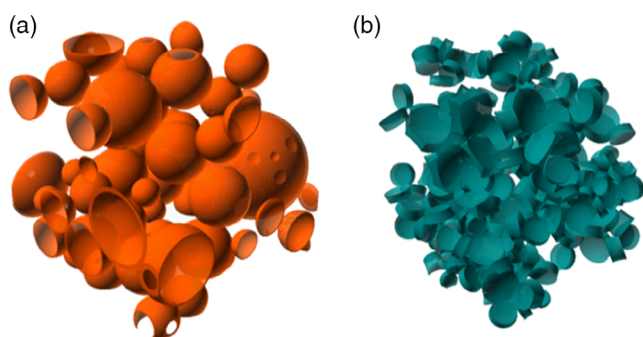


Figure 6. Binder distribution within the porous structure, by a) binder shells and b) binder bridges.

of three structures generated: a) One with shells, b) one with bridges, and c) one with a combination of shells and bridges.

In order to discuss which kind of binder distribution might be more realistic, the particles are removed from both structures in **Figure 6a,b**, so that only the binder shells or bridges are shown.

Wang et al.,^[40] Chong et al.,^[41] and Lim et al.^[42] showed that the BCB mixture is concentrated near to the contact points between two adjacent particles, caused by the capillary effect of the binder solution, which corresponds to a binder distribution in the form of binder bridges, as can be seen on the left-hand side of **Figure 7**. Indrikova et al.,^[43] Pfaffmann et al.,^[38]

Bauer et al.,^[36] and Almar et al.^[37] showed in their work that the BCB fraction which completely covers the AM is negligible, compared with the fraction that forms bridge-like structures (as can be seen on the right-hand side of **Figure 7** for the CB phase). Based on the work of these authors, it can be concluded that a BCB network like the generated binder-bridge distribution in this work (compare **Figure 6b**) is a very good resemblance of the BCB distributions in electrodes shown in **Figure 7**.

In the case of the binder shells, the binder is mainly distributed near the AM surface, and this leads to a reduced overlap in comparison to the binder bridges. The overlap of the binder bridges results in an uneven binder distribution, which is comparable to binder networks in real electrodes, according to Almar et al., Bauer et al. and Pfaffmann et al.^[36–38] In addition, several crossing binder bridges lead to a partial covering of the particle, which, in turn, leads to shell-like binder structures. Another aspect to be considered is the surface covering of the AM by the BCB mixture. In the case of the binder shells, there is nearly a complete surface coverage, while binder bridges lead to a partial coverage. The surface coverage of the AM particles with BCB mixture can be calculated with an implemented contact area calculation. In the case of binder bridges, the average surface coverage of the particles by the BCB mixture is about 35–40%, which almost corresponds to the literature value of 40% according to Yoo et al.^[44] In summary, the resulting binder distribution of the binder bridges enables a more precise replication of real

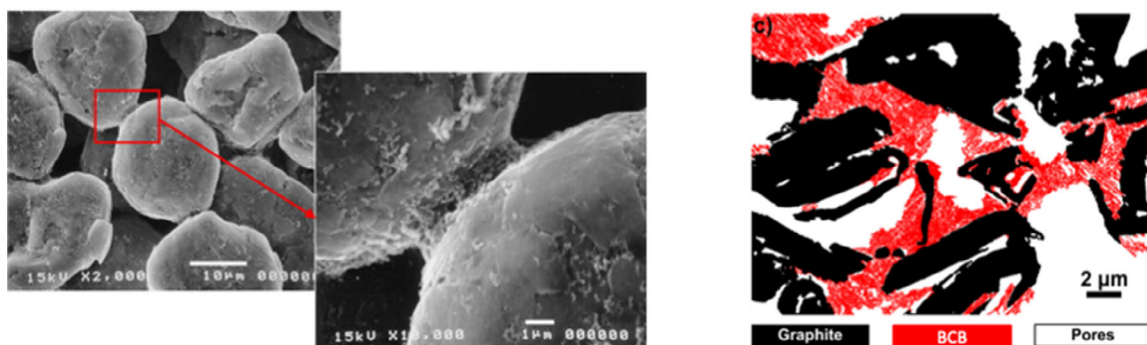


Figure 7. Left, illustration of a SEM image of binder bridges between adjacent particles. Reproduced with permission.^[40] Copyright 2008, Elsevier. Right, ESB image of the distribution of the graphite AM, CB, and pore space. Reproduced with permission.^[38] Copyright 2017, Elsevier.

binder distributions found in literature and will, therefore, be the focus in the following sections.

When the structure generation routine has finished, the pre-processing phase starts. The files of each particle and binder bridge are transferred to the meshing tool snappyHexMesh^[45] to create a discretization grid of the whole porous electrode structure. All grid cells that are not assigned to the particles or binder phase are defined as electrolyte. After the grid generation, the initial and boundary conditions and the coupling conditions between the different phases/regions are defined. A first-order boundary condition (Neumann condition: “fixedValue”), i.e., a constant temperature of 323 K (top) and 273 K (bottom), is selected for the upper and lower limits of the system volume. The arithmetic mean of these two temperatures for the initial condition is set for the entire system. The lateral system limitations are considered adiabatic, therefore, a second type of boundary condition (Dirichlet condition: “zeroGradient”) is applied. The coupling condition “turbulentTemperatureCoupledBaffleMixed” of OpenFOAM is chosen for the contact areas of the regions. The OpenFOAM extension “swak4Foam” is used for the automatic calculation of the contact areas. In addition to the calculation of the contact areas between the particles, the areas between particles and binder, particles and electrolyte, and particles and current collector and separator are also calculated.

2.2. Definition and Determination of the Effective Thermal Conductivity

This section describes the definition and calculation method of the effective thermal conductivity for porous electrodes. A temperature gradient in solids and static fluids induces heat transport by thermal conduction. According to the second law of thermodynamics, heat in macroscopic processes always flows from a higher temperature level to a lower temperature level. The stationary heat flux density \vec{q} for steady-state conditions can be described with the Fourier heat conduction equation, where λ represents the thermal conductivity of the material and ∇T the temperature gradient^[46]

$$\vec{q} = -\lambda \cdot \nabla T \quad (1)$$

In the case of 1D heat conduction, the vectorial Equation (1) reduces to the scalar Equation (2), where A is the cross-sectional area normal to the heat flow direction and s is the path length in the heat flow direction:^[46]

$$\dot{Q} = -\lambda \cdot A \cdot \frac{dT}{dx} = -\frac{\lambda}{s} \cdot A \cdot (T_2 - T_1) \quad (2)$$

The case of stationary, 1D heat conduction described in Equation (2) is shown schematically in **Figure 8**. The shaded system boundaries are adiabatic as no heat flows over the lateral surfaces.

The area shown in green (see Figure 8, left) represents a homogeneous solid or a static fluid which has a constant thermal conductivity. In this case, heat transfer by convection can be neglected. However, the area can also be described as a black box, which represents a heterogeneous system, such as the porous electrode coating (see Figure 8, right). As a result, due to the heterogeneous structure, we speak of an effective thermal conductivity, which consists of contributions of various components with different material and transport properties. If Equation (2) is applied, an effective thermal conductivity must be assigned to the heterogeneous electrode structure. Conversely, if the temperature difference applied, the stationary heat flow and the geometrical dimensions of the structure are known, the effective thermal conductivity can be determined. In this work, a thermal simulation of the porous electrode structure is carried out by specifying a defined temperature difference as a boundary condition to determine the stationary heat flow through the structure. The effective thermal conductivity of the porous electrode coating is then calculated using Equation (3)

$$\lambda_{\text{eff}} = \frac{\dot{Q} \cdot s}{A \cdot (T_1 - T_2)} \quad (3)$$

2.3. Numerical Solution Method

The numerical method for calculating the heat flow through the porous structure is presented in this section. This work uses the open-source simulation software OpenFOAM, which is based on the finite volume method, to determine the steady-state heat

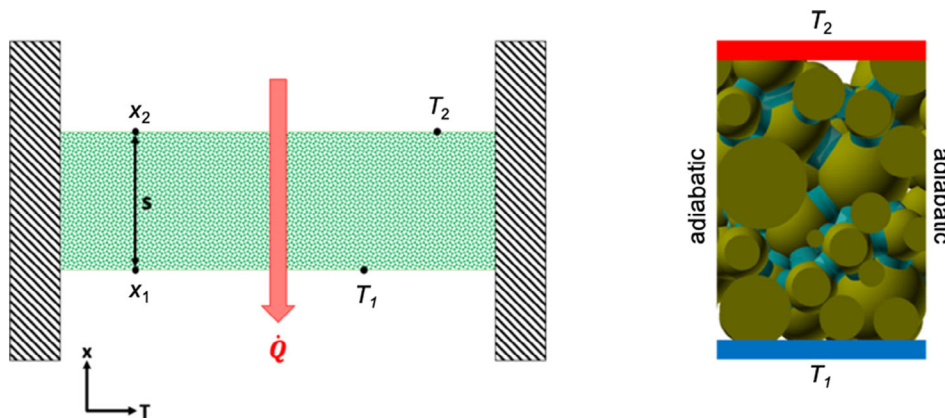


Figure 8. Left, schematic diagram of stationary heat conduction, heat flow from higher temperature T_2 (top) to lower temperature T_1 (bottom). Right, porous electrode structure as a black box system.

flow. The basis is the conservation equation for the transport of a scalar quantity ϕ in the general form, according to Equation (4):^[47]

$$\underbrace{\frac{\partial}{\partial t}(\rho\phi)}_{\text{temporal change}} + \underbrace{\nabla \cdot (\rho\phi\vec{v})}_{\text{convection}} = \underbrace{\nabla \cdot (\Gamma\nabla\phi)}_{\text{diffusion}} + \underbrace{S_\phi}_{\text{source}} \quad (4)$$

Some assumptions can be made to simplify Equation (4) for the investigation of the porous electrode structures. The term of the temporal change of Equation (4) is omitted, because only steady-state simulations are performed. Furthermore, the electrolyte is assumed to be static fluid ($\vec{v} = 0$), since flows of the fluid within the electrodes can be neglected, whereby the convection term also becomes zero. Finally, the source term is omitted on the right-hand side, since the numerical simulations are not intended to depict real thermal processes within the porous electrodes but only to determine an effective transport quantity. Thus, the general conservation equation is simplified to Equation (5), in which only the diffusion term is present:

$$\nabla \cdot (\Gamma\nabla\phi) = 0 \quad (5)$$

The stationary simulation of the porous electrode structure is performed with the solver “chtMultiRegionFoam”,^[48] which can calculate the heat transfer between several fluid and solid regions by solving the conservation equation for the transport quantity of the specific enthalpy h . The proportionality factor Γ corresponds to the material-dependent thermal diffusivity a , which in OpenFOAM, contrary to the usual convention $a = \lambda/(\rho \cdot c_p)$, is defined as the ratio of thermal conductivity λ to specific heat capacity c_p , see $a = (\lambda/c_p)$.

2.3.1. Postprocessing

After completing the simulation, the post-processing tool “wallHeatFlux” from OpenFOAM is used to calculate the incoming and outgoing heat flows in each region (particle, binder bridges, and electrolyte). The total heat flows through the hot (top) and cold side (bottom) of the structure are calculated automatically to determine the effective thermal conductivity. The thermal conductivity is then determined according to Fourier’s heat conduction, Equation (3).

3. Analytical Model

The following section deals with an analytical model approach to describe the effective thermal conductivity of porous electrode coatings. Many analytical approaches have been developed to model classical porous particle structures, such as the Maxwell–Eucken,^[49,50] effective medium theory,^[51–53] and Krischer model.^[54] The Maxwell–Eucken model represents the lower and the upper limit of the effective thermal conductivity of porous particle beds. Thereby, it is only possible to differentiate between a solid phase and a fluid phase, where one of the two phases can be considered as continuous and the other as disperse.^[49,50] The disperse phase is uniformly distributed in the continuous phase in the manner of spheres.^[49,50] A further

development is the effective medium theory model, which is a mixture of the upper and lower limits of the Maxwell–Eucken model and can, thus, contain more than two phases that are stochastically distributed.^[51–53] In the Krischer model, on the other hand, thermal resistors are mixed and arranged in series and/or parallel connections.^[54] Several phases can also be considered in this model, but it provides no structural information. The models mentioned above are unsuitable for describing the thermal conductivity of porous electrode structures, as none of them contain structural information, such as the particle shape, particle contact areas, or binder distribution. In contrast, the ZBS model^[32–34] represents a further development of the Krischer model, which takes into account the particle shape and preferred thermal heat-conduction pathways. In the following, a self-developed extension of the ZBS model regarding porous electrode coatings is derived in detail. Input parameters are bulk thermal conductivities and volume fractions of the AM λ_{AM}, v_{AM} , the BCB mixture λ_{BCB}, v_{BCB} and the fluid phase λ_F, ϕ , as well as the particle distance parameter c and the particle contact area parameter α . These parameters are assumed to be known for the following derivation, according to Equation (6):

$$\lambda_{\text{eff}} = f(\lambda_{AM}, \lambda_{BCB}, \lambda_F, v_{AM}, v_{BCB}, \phi, c, \alpha) \quad (6)$$

The three main thermal heat-conduction pathways in a porous electrode are shown schematically on the left-hand side of **Figure 9**. In pathway 1, heat conduction takes place through the fluid/electrolyte phase and in pathway 2, because of the contact areas of the AM particles. Pathway 3 represents a mixture of the fluid, AM and BCB. The right-hand side of Figure 9 shows the unit cell of the thermal resistance network of the extension to the ZBS model developed in this work for porous electrodes. Hereby, a section of a rotationally symmetrical basic structure is illustrated. Thereby, a parallel connection of the three main heat-conduction pathways is assumed. In addition, the three main heat-conduction pathways are weighted differently due to structural parameters, such as porosity, tortuosity, and the particle contact area. Here, pathway 3 contains the structural information, such as the particle shape (phase 3) and the geometry of the binder distribution (phase 4, 6) representing binder bridges. This structure forms the basis for deriving an extended form of the ZBS model by transforming its phases and their connections into a resistor network. The latter will be described next.

The effective thermal conductivity of the resistance network is described by a parallel connection of the three main heat-conduction pathways (see Equation (7)), considering the corresponding radii of the cylinder cut-out.

$$\lambda_{\text{eff}} = (1 - r_2^2) \cdot \lambda_{\text{path1}} + (r_2^2 - r_3^2) \cdot \lambda_{\text{path2}} + r_3^2 \cdot \lambda_{\text{path3}} \quad (7)$$

Pathway 1 corresponds to the thermal conductivity of the fluid $\lambda_{\text{path1}} = \lambda_F$ and pathway 2 to the conductivity of the AM $\lambda_{\text{path2}} = \lambda_{AM}$. The ratio of the effective thermal conductivity of the electrode λ_{eff} and the thermal conductivity of the fluid λ_F is formed to determine the radius r_2 . In the case of a nonthermally conducting particle bed $\lambda_S/\lambda_F \rightarrow 0$, the diffusion processes occurring in the fluid can be regarded as analogous, whereby Equation (8) results:

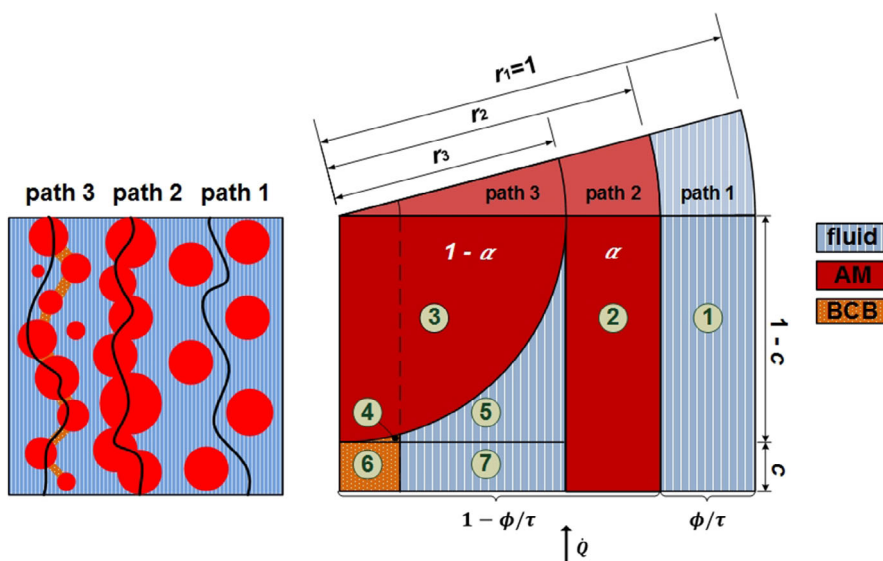


Figure 9. Left, illustration of the three main heat-conduction pathways in porous electrodes: Pathway 1 heat conduction through the fluid, pathway 2 heat conduction through the AM, and pathway 3 heat conduction through a mixture of fluid, AM, and BCB. Right, illustration of the thermal resistance network of the extended ZBS model for porous electrodes for phases 1 to 7.

$$\lim_{\lambda_s/\lambda_F \rightarrow 0} \frac{\lambda_{\text{eff}}}{\lambda_F} = \frac{D_{\text{eff}}}{D_F} = \frac{\phi}{\tau_F} = \nu_1 = 1 - r_2^2 \quad (8)$$

$$\lambda_{\text{path3}} = \frac{1}{(1-c)/\lambda_{3,4,5} + c/\lambda_{6,7}} \quad (13)$$

Regarding the limit value, this results in the ratio of porosity ϕ and tortuosity of the fluid τ_F after the well-known Knudsen diffusion,^[55] which also corresponds to the volume fraction ν_1 of pathway 1. The radius r_2 can be determined with this set of equations:

$$r_2 = \sqrt{1 - \frac{\phi}{\tau_F}} \quad (9)$$

The tortuosity of the fluid phase τ_F can be described by different approaches, such as the Bruggemann formula.^[3,31] Here, the tortuosity τ_F is described by the ZBS approach,^[32-34] according to Equation (10):

$$\tau_F = \frac{\phi}{1 - \sqrt{1 - \phi}} \quad (10)$$

In addition, the radius r_3 is required, which is calculated from the volume fraction ν_2 of pathway 2. The volume fraction ν_2 can be described as an expression of the total volume fraction of the AM ν_{AM} and the parameter α , according to Equation (11). Then, by transformation, Equation (12) yields the radius r_3 :

$$\nu_2 = \alpha \cdot \nu_{\text{AM}} = (r_2^2 - r_3^2) \quad (11)$$

$$r_3 = \sqrt{r_2^2 - \alpha \cdot \nu_{\text{AM}}} \quad (12)$$

In a next step, the thermal conductivity of pathway 3 can be expressed by a series connection of phase 3, 4, and 5 and phase 6 and 7 according to Equation (13). The parameter c corresponds to the mean particle distance resulting due to the length of a binder bridge.

For reasons of simplification, the radius r and the height z of the inner cylindrical section of the resistance network in **Figure 10** are normalized to the value one. According to Equation (14), the thermal conductivity of phase 6 and 7 can be described via a parallel connection, with normalized radius r_{BCB} of the binder bridge mentioned above.

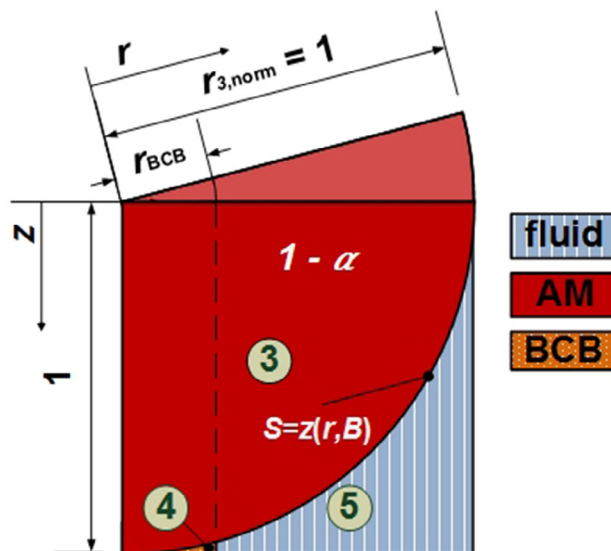


Figure 10. Illustration of phases 3, 4, and 5 with normalized radius r and height z . Here, phase 3 represents the shape of the AM particle, described according to the surface Equation (15).

$$\lambda_{6,7} = r_{BCB}^2 \cdot \lambda_{BCB} + (1 - r_{BCB}^2) \cdot \lambda_F \quad (14)$$

The boundary of phase 3 is described via the surface Equation (15) and corresponds to the shape of the AM particle, which is varied using the so-called particle shape factor B . If $B = 0$, the particle boundary and the z -axis coincide and the AM content of the particle v_3 is nearly zero. For $B = 1$, the particle becomes a sphere and for $B \rightarrow \infty$, the AM occupies the entire cylinder volume in Figure 10.

$$S(r, z, B) = r^2 + \frac{z^2}{(B - (B - 1) \cdot z)^2} = 0 \quad (15)$$

In order to determine the unknown shape factor B , the volume fraction $v_{3, \text{norm}}$ is normalized to the system volume fraction $v_{3,4,5}$ according to Equation (16). By means of Equation (15) and (16), the shape factor B can be calculated iteratively for a known volume fraction of the AM v_{AM} .

$$v_{3, \text{norm}} = \frac{v_3}{v_{3,4,5}} = \frac{(1 - \alpha) \cdot v_{AM}}{(1 - c) \cdot r_3^2} = \int_0^1 2 \cdot r \cdot z(r, B) dr \quad (16)$$

In a last step, the radius r_{BCB} of the binder bridge is required. Therefore, the volume fraction v_4 and v_6 of the binder phases 4 and 6 are calculated according to Equation (17) and (18):

$$v_4 = (1 - c) \cdot r_3^2 \cdot \int_0^{r_{BCB}} 2 \cdot r \cdot (1 - z(r, B)) dr \quad (17)$$

$$v_6 = c \cdot r_3^2 \cdot r_{BCB}^2 \quad (18)$$

The sum of the volume fraction v_4 and v_6 gives the total fraction of the BCB phase v_{BCB} . The normalized radius r_{BCB} of the binder bridge can be determined iteratively by inserting Equation (17) and (18) in (19):

$$v_{BCB} = v_4 + v_6 \quad (19)$$

The thermal conductivity $\lambda_{3,4,5}$ of phase 3, 4, and 5 can then be calculated using Equation (20) and, finally, the effective thermal conductivity λ_{eff} of the porous electrode results.

$$\lambda_{3,4,5} = 2 \cdot \pi \cdot \left(\int_0^{r_{BCB}} r \cdot \frac{1}{\frac{z(r, B)}{\lambda_{AM}} + \frac{(1 - z(r, B))}{\lambda_{AM}}} dr + \int_{r_{BCB}}^1 r \cdot \frac{1}{\frac{z(r, B)}{\lambda_{AM}} + \frac{(1 - z(r, B))}{\lambda_F}} dr \right) \quad (20)$$

4. Results and Discussion

In the following, the numerical and analytical models for determining the effective thermal conductivity of electrode coatings are verified against each other. This is done by a series of selected simulation studies, in which the thermal conductivity of the AM, the composition, and the fraction of the BCB mixture are varied.

Assuming the identical structural parameters for the numerical and analytical model is attempted as far as possible. Thereby, the studies for the porous anode and cathode coatings are performed for discharged cells at begin-of-life, which corresponds to a State of Charge of 0%. Furthermore, the thermal resistance caused by the SEI formation at the surface of the porous anode coatings is neglected in this work. First, the thermal transport parameters of the individual electrode components and the particle size distribution required for the structure generation of the numerical model are discussed. Table 2 lists the bulk material parameters of the individual phases necessary for modeling, including the literature references. If several references are indicated, the mean value of these is calculated.

Since the BCB phase is considered homogeneous, the thermal conductivity of the mixture can be calculated according to Hamilton and Crosser,^[67] with the necessary bulk properties of the BCB phase (see Table 2). The literature data^[65,68–70] which contain thermal conductivity values as a function of the CB fraction for the homogeneously considered BCB mixture are used for the parameterization of the model. Thus, a parameterization factor for the model of $f = 3.2$ results. Table 3 shows the thermal conductivity of the homogeneous BCB mixture as a function of the CB fraction.

The particle size distribution according to Ender^[71] is used for the anode coating, whereas the cathode coating is generated by a particle size distribution from Almar et al.^[37] Both particle size distributions were determined using computer-aided electrode reconstructions based on focused-ion beam tomography images. The numerical structures generated in this work, with the particle size distributions mentioned above, have average specific surface areas of $1.2 \mu\text{m}^{-1}$ (anode structures) and $1.1 \mu\text{m}^{-1}$ (cathode structures). These values show a good agreement with the literature values of 0.7 to $1.3 \mu\text{m}^{-1}$ according to Almar et al.^[37] Structures with system dimensions of $15 \times 15 \times 20 \mu\text{m}$ are generated, which have a number of

Table 2. Listing the thermal transport parameters of the components of the porous electrode coatings.

Material	Thermal conductivity [W m ⁻¹ K ⁻¹]	Density [kg m ⁻³]	Heat capacity [J kg ⁻¹ K ⁻¹]
Graphite	139 ^[2,30,56]	2260 ^{a)}	715 ^{a)}
LCO	6 ^[57–59]	5028 ^{a)}	716 ^{a)}
Binder PVDF (B)	0.20 ^[60–63]	1809 ^{a)}	1114 ^{a)}
Carbon black	23.85 ^[64–66]	2260 ^{a)}	650 ^{a)}
LP30	0.18 ^{a)}	1286 ^{a)}	1648 ^{a)}

^{a)}Experimentally determined value.

Table 3. Compositions and thermal conductivities of the BCB mixture, calculated according to Hamilton and Crosser,^[67] with a parameterization factor $f = 3.2$.

Fraction in wt%	Binder PVDF	90	70	50	30	10	3
	CB	10	30	50	70	90	97
λ_{BCB} in W m ⁻¹ K ⁻¹		0.25	0.40	0.66	1.25	3.81	10.00

3 million grid cells, for the following simulations. System volumes of larger dimensions do not show significant changes in the effective thermal conductivity.

The analytical model derived in Section 3 depends on the mean particle distance, which is reflected in the parameter c . For this purpose, the numerical tool is utilized to generate, first, a series of reference structures as a function of porosity and, afterward, their effective thermal conductivity is calculated. The numerically calculated thermal conductivities are approximated to the analytical model applying the method of least squares, which results in the porosity-dependent parameterization factor c :

$$c = 0.008 \cdot \exp(4.21 \cdot \phi) \quad (21)$$

The expression of the particle distance parameter c shown in Equation (21) is used for the following comparisons of the numerical with the analytical model. Furthermore, no particle contact is considered in the simulation studies, which is why the particle contact parameter α is set to zero.

In the first study, the influence of the thermal conductivity of the AM on the effective thermal conductivity is investigated. For this purpose, the thermal conductivity of the AM is varied and simulations are performed with three anode and three cathode structures each of different porosities but identical compositions (the solid volume consists of 10 vol% BCB and 30 wt.% of the BCB is CB). LP30 is chosen as the electrolyte. The thermal conductivity of the AM is varied from $138.6 \text{ W m}^{-1} \text{ K}^{-1}$ (anode, isotropic average graphite) and $6 \text{ W m}^{-1} \text{ K}^{-1}$ (cathode, LCO) by $\pm 20\%$ and $\pm 50\%$, respectively. Furthermore, a generic

minimum of $10 \text{ W m}^{-1} \text{ K}^{-1}$ (anode) and a maximum of $20 \text{ W m}^{-1} \text{ K}^{-1}$ (cathode) are investigated. **Figure 11** shows the simulation results of the variation study of the thermal conductivity of the anode AM on the left-hand side, all three porosities investigated show a minor influence on the effective thermal conductivity. A significant reduction in the effective thermal conductivity can be observed only for the generic minimum of $10 \text{ W m}^{-1} \text{ K}^{-1}$. The limitation of heat transport is, therefore, not attributed to the thermal conductivity of the AM but to the conductivity of the BCB mixture and the electrolyte. The slight difference in the effective thermal conductivity of the anode and cathode coating can also be explained by the aforementioned inhibitions. The electrolyte and the BCB phase have a very low thermal conductivity of 0.18 and $0.4 \text{ W m}^{-1} \text{ K}^{-1}$ (30 wt% CB), compared to the AM phase (compare Table 2, 3, and Figure 11). The lowest thermal resistances, in this case assigned to the electrolyte and the BCB phases, lead to a significant reduction in the effective thermal conductivity despite of the higher thermal conductivity of the AM of the anode coatings. Therefore, similar results are obtained for both the anode and cathode coatings. This is also confirmed by the illustrated results in **Figure 12**, where the increase in the thermal conductivity of the BCB phase and thus a reduction of the limiting thermal resistance leads to significant difference in both the anode and cathode coatings caused by the higher conductivity of the anode coating. The results of the cathode structures (on the right-hand side, according to Figure 11) show, in contrast to the anode structures, an influence of the AM thermal conductivity, which depends on the porosity. This is caused by the low thermal conductivity of the AM of the cathode compared to the anode. More

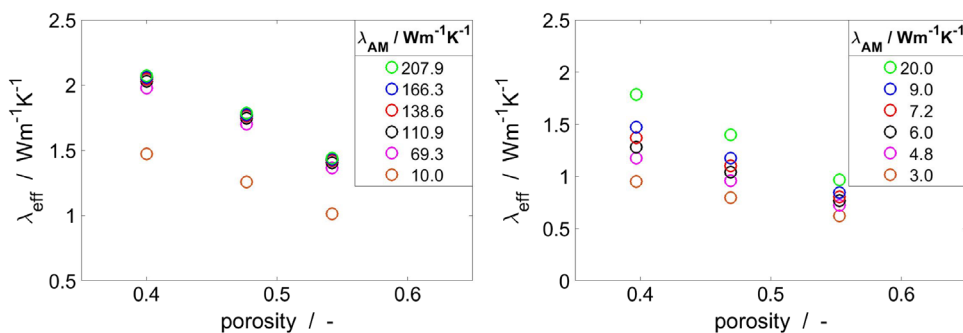


Figure 11. Influence of the thermal conductivity of the AM on the effective thermal conductivity: Left, anode structures, and right, cathode structures.

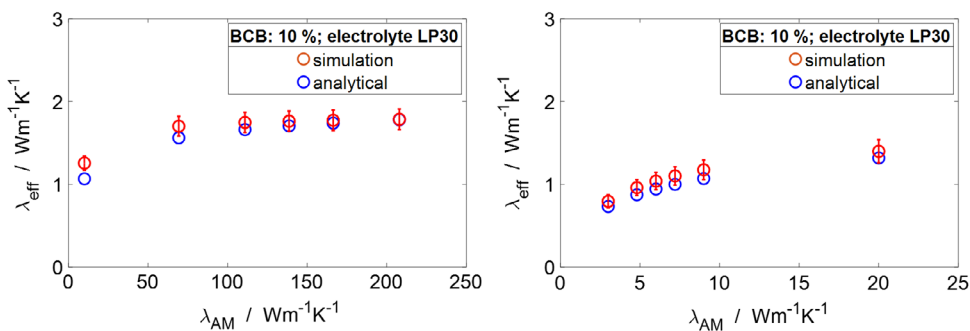


Figure 12. Comparison of the effective thermal conductivity of the numerical and analytical model as a function of the AM thermal conductivity: Left, anode structure (porosity 0.48), and right, cathode structure (porosity 0.47).

heat-transport pathways through the AM particles exist at lower porosities, so that an increase in the AM thermal conductivity has a greater effect.

The effective thermal conductivity for a mean porosity of about 0.48 from Figure 12 is plotted over the thermal conductivity of the AM for both the anode and the cathode coatings. In addition, the results of the analytical model are also shown for comparison in Figure 12. Both models predict almost the same trend for the effective thermal conductivity. The effective thermal conductivity of the coatings increases strongly at low AM thermal conductivities, whereas the slope of the curve decreases at higher active thermal conductivities. Due to the underlying stochastics in the structure generation, the anode and cathode coatings show varying effective thermal conductivities, despite identical compositions and particle size distributions. Consequently, the numerical results show an average uncertainty of 7% for the coatings. The average deviation from the mean values of the simulation results compared to the results of the analytical model is about 4% for the anode and 8% for the cathode coating. When the stochastic uncertainty of structure generation is included, there are only minor deviations between the results.

The influence of the thermal conductivity of the BCB mixture on the effective thermal conductivity is investigated in the following study. The BCB mixture is considered as a homogeneous phase and modeled in the manner of binder bridges. The thermal conductivity of the mixture is determined using the Hamilton and Crosser model, according to Table 3. Usual mass fractions of CB in the BCB mixture are 30–50 wt%. The generic proportions of 10, 70, 90, and 97 wt% are also considered to estimate the effects of the CB. The value of 97 wt% was chosen so that the thermal conductivity of the BCB mixture has a generic maximum value of $10 \text{ W m}^{-1} \text{ K}^{-1}$. Three structures of different porosities with a BCB fraction of about 10 vol% related to the total solid volume are regarded for the anode and cathode coating. **Figure 13** illustrates the simulation results for the anode (left) and the cathode structures (right); the effective thermal conductivity is plotted over the porosity. The simulation results show that the thermal conductivity of the BCB mixture has a great influence on the effective thermal conductivity of anode and cathode structures. The binder bridges lead to thermal conduction pathways between the particles. A higher conductivity of the binder bridges results in better conducting transport pathways through the solid phase and, thus, in an increase of the effective thermal conductivity of the electrode structures. This effect

occurs more strongly with lower porosity, i.e., with increased solid content, which is confirmed by the simulation results in Figure 13. The effective thermal conductivity increases very strongly with increasing thermal conductivity of the BCB mixture, especially for the anode structures, as the high AM conductivity of graphite contributes additionally to improved heat transport. In contrast, the increase in effective thermal conductivity is generally lower in the cathode structures, as the effect of the improved heat-transport pathways is less pronounced here due to the lower thermal conductivity of the AM. Nevertheless, the effective thermal conductivity increases significantly with the conductivity of the BCB mixture.

The influence of the composition of the BCB consisting of polyvinylidene fluoride (PVDF) and CB is discussed in the following. For this purpose, the results of the anode and cathode structures for the mean porosity according to Figure 13 are chosen and, therefore, plotted in **Figure 14** over the CB fraction. The same color coding as that shown in Figure 13 is used. Furthermore, the results of the numerical model are compared with the analytical model for verification. Both models show a very good agreement and an exponential increase in effective thermal conductivity with the increasing CB fraction. The effective thermal conductivity of the anode coating shows a significantly higher gradient with an increase in the CB fraction compared to the cathode coating. The numerical simulation results show an uncertainty of 7% for the anode and 9% for the cathode coating due to the stochasticity of the structure generation. The average deviation from the mean values of the simulation results compared to the results of the analytical model is about 4% for the anode and 11% for the cathode coating. There are only minor deviations between the results when including the stochastic uncertainty of structure generation. As explained at the beginning, the usual CB fraction in the mixture lies within a range of 30 to 50 wt%. In summary, Figure 14 shows a significant improvement in the effective thermal conductivity for this range, with increasing CB fraction.

In the next study, the BCB fraction will be increased from 5 vol%, in relation to the solid volume, to 20% for anode and cathode structures, with a constant CB fraction of 30 wt%. LP30 is again chosen as the electrolyte. The results for both the numerical and analytical model are shown in **Figure 15**. The analytical and numerical model again show a very good agreement. On the one hand, the solid phase increases with the increasing BCB fraction and, on the other hand, further heat-conduction pathways

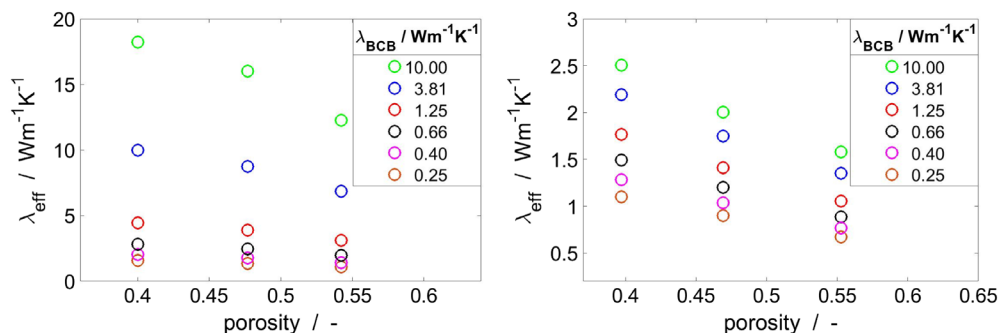


Figure 13. Influence of the thermal conductivity of the BCB mixture on the effective thermal conductivity: Left, anode structures, and right, cathode structures.

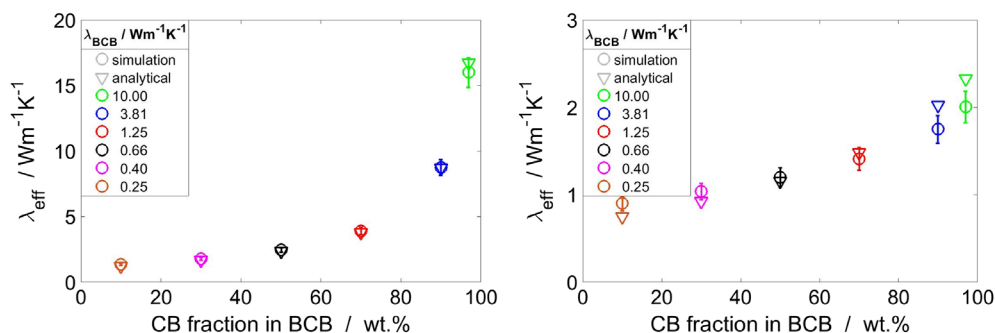


Figure 14. Influence of the CB fraction in the BCB mixture on the effective thermal conductivity of structures of medium porosity: Left, anode structure (porosity 0.48), and right, cathode structure (porosity 0.47).

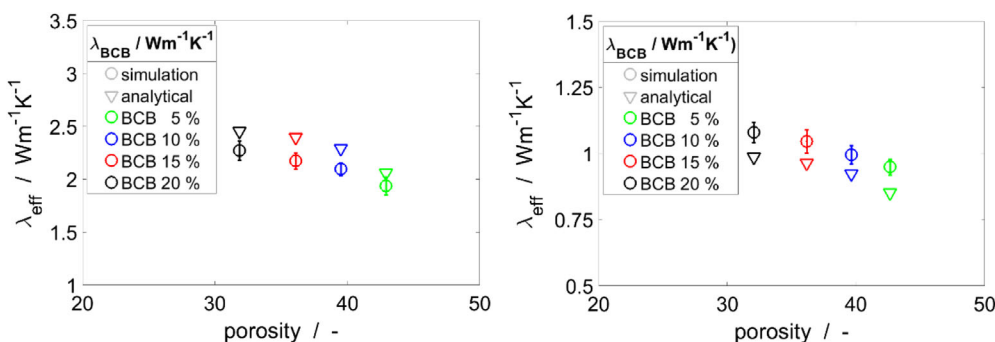


Figure 15. Influence of the BCB fraction on the effective thermal conductivity: Left, anode coating, and right, cathode coating.

are formed (see **Figure 16**), which leads to an increase in the effective thermal conductivity. The increase results from the reduction of the electrolyte phase, which has a lower thermal conductivity compared to the BCB phase. The uncertainty of the structure generation is reflected in a mean uncertainty of 4% for the anode and cathode coatings. The average deviation from the mean values of the simulation compared to the results of the analytical model is about 8% for both the anode and cathode

coatings. Considering the stochastic uncertainty, there are minimal deviations again between the analytical and the numerical model. Compared to the study in which the CB fraction was increased, a smaller increase in the effective thermal conductivity can be recognized.

Finally, a validation of the simulation data is carried out using the literature data listed in Table 1. The literature data vary between 0.89 and $3.2 \text{ W m}^{-1} \text{ K}^{-1}$ for the anode coating (graphite)

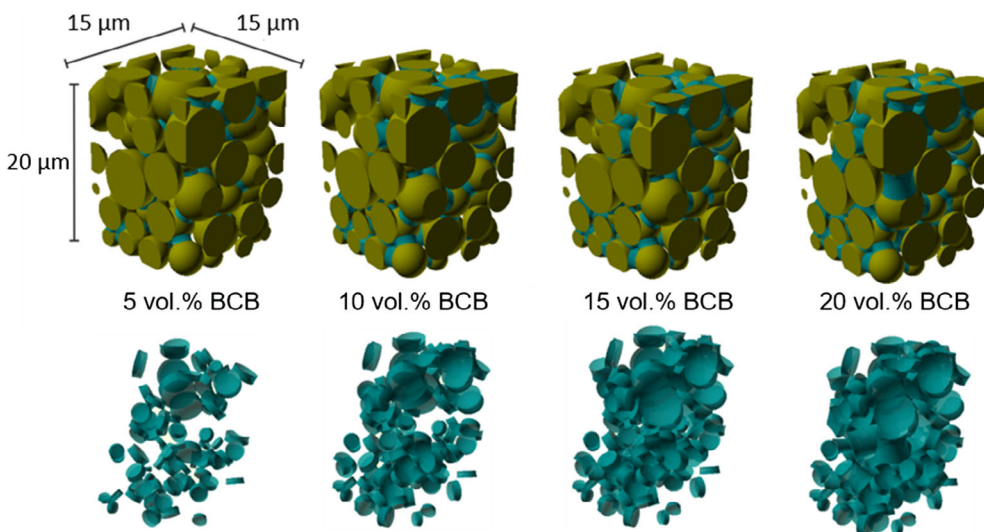


Figure 16. Illustration of the electrode coating and the BCB network with an increasing BCB mixture from 5 to 20 vol%.

Table 4. Comparison of the experimentally, numerically, and analytically determined effective thermal conductivity of the electrode coatings of cell A and B at room temperature. Helium was chosen as the filling medium for the pore spaces.

	Experiment in $\text{W m}^{-1} \text{K}^{-1}$		Simulation in $\text{W m}^{-1} \text{K}^{-1}$		Analytical in $\text{W m}^{-1} \text{K}^{-1}$	
	Anode	Cathode	Anode	Cathode	Anode	Cathode
Cell A	2.46 ± 0.31	0.70 ± 0.07	2.41 ± 0.12	0.82 ± 0.06	2.52	0.86
Cell B	2.74 ± 0.45	1.01 ± 0.14	2.64 ± 0.18	0.87 ± 0.04	2.50	0.90

and 0.82 and $1.58 \text{ W m}^{-1} \text{K}^{-1}$ for the cathode coating (LCO). These values are in a very good agreement with the simulation data, which range from 1.2 to $3 \text{ W m}^{-1} \text{K}^{-1}$ for the anode coating and 0.6 to $1.8 \text{ W m}^{-1} \text{K}^{-1}$ for the cathode coating. Typical compositions of common coatings were chosen for the comparison and, thus, the simulation results of the variation of the CB fraction between 10 and 50 wt\% in the BCB mixture and the study of the variation of the volume fraction of the BCB phase were used.

Table 4 shows the experimentally determined effective thermal conductivities for both the anode and cathode coatings for two commercial cells A and B. For the experiments cells at begin-of-life were used with a State of Charge of 0% . The cells were disassembled in an argon atmosphere within a glove box system, so that the anodes and cathodes could be used for the experimental determination of the effective thermal conductivity of their porous coatings. The experimental results were determined at a temperature of $25 \text{ }^\circ\text{C}$ by laser flash analysis, with helium as filling fluid instead of electrolyte. Helium was preferred due to the volatility of electrolytes and their incompatibility with the measuring method. Further details of the measuring method can be found in the Supporting Information. The structure parameters and the composition of the cells were analyzed by images of the focused ion beam tomography and, in a next step, transferred to the structure-generation routine as input parameters. The thermal parameters for the bulk materials from Table 2 and 3 and the thermal transport properties of helium,^[28] as a filling medium were selected for the simulation of the reconstructed coatings. The comparison of the experimental with the numerical and analytical results in Table 4 shows a very good agreement, consequently, the numerical and analytical model are considered validated.

5. Conclusion and Outlook

In this work, a numerical and an analytical model are introduced which describe the effective thermal conductivity of porous electrode coatings. An automated simulation tool based on a detailed generic 3D geometry was developed for the numerical approach, which considers the morphological parameters and thermal bulk material properties of real electrode structures. Nonlinear systems of transport equations are discretized by the finite volume method and solved with a suitable solver from the open-source package OpenFOAM to calculate the effective thermal conductivity. The analytical model approach based on thermal resistance

networks according to ZBS was fundamentally developed further for porous electrode coatings by introducing parameters such as particle contact areas, particle distances, and the BCB phase and its distribution. The goal was to develop a fast and precise model which shows a high agreement with the numerical simulation results over a wide parameter range. Several studies were carried out by varying the AM conductivities, conductivities of BCB mixtures and compositions of these mixtures, as well as solid fractions of the individual electrode components. The studies show that an increase in the AM bulk thermal conductivity of the anode coating has no significant influence on the effective thermal conductivity of the porous coating. This contrasts with the AM of the cathode, which has a fundamentally lower thermal conductivity and, therefore, more room for improvement. The variation in thermal conductivity of the BCB mixture shows a great influence on the effective thermal conductivity of both the anode and cathode coatings. An increase in the conductivity of this phase can be achieved by new types of binders, carbon nanotubes instead of CB, or simply by increasing the CB content. In the last study, the BCB fraction was increased at a constant AM volume fraction, which resulted in a higher effective thermal conductivity of the coatings. The increase in thermal conductivity of the BCB mixture has the greatest influence compared to the studies shown, since the thermal transport pathways formed by the binder are the limiting factor. Altogether, the studies showed a significant dependence of the effective thermal conductivity on the porosity. In comparison to the numerical simulation, the analytical model showed the same dependencies and correlations and only slight deviations were noticeable; therefore, the models can be regarded as verified. Finally, the numerical model was validated using literature and our own measurement data. The presented models can also be applied to different anode and cathode coatings, consisting of different AM fractions and materials as well as BCB fractions and distributions. Thereby, with the aforementioned structure-generation routine, the AM amount and the shape of the AM particles can be varied and also the thermal transport properties can be changed according to the required AM, as shown in Figure 11 and 12. The binder fraction is generated according to a user-defined input parameter and different binder distributions can be realized by combinations of binder shells and binder bridges, as shown in Figure 5. Furthermore, the thermal transport properties of the binder or BCB phase can also be changed depending on the electrode coating. Finally, it is possible to vary the thermal properties of the electrolyte. Therefore, it is possible to describe a broad spectrum of different anode and cathode compositions. In future, the models can be extended by current collectors and separators so that complete electrode stacks or unit cells can be simulated or calculated. In addition, the influence of the orientation of ellipsoid-shaped particles on the effective thermal conductivity can be investigated and transferred to the analytical model.

Supporting Information

Supporting Information is available from the Wiley Online Library or from the author.

Acknowledgements

The authors thank Dominic Becker and Sabrina Herberger for their invaluable support of this work. This work was funded by the Deutsche Forschungsgemeinschaft (DFG) within the framework of the research training group SIMET (281041241/GRK2218). Open access funding enabled and organized by Projekt DEAL.

Conflict of Interest

The authors declare no conflict of interest.

Keywords

effective thermal conductivity, lithium-ion cells, microstructure, porous electrodes, simulation

Received: June 17, 2020

Revised: July 16, 2020

Published online:

- [1] H. Maleki, J. Robert Selman, R. B. Dinwiddie, H. Wang, *J. Power Sources* **2001**, 94, 26.
- [2] C. Sangrós, C. Schilde, A. Kwade, *Energy Technol.* **2016**, 4, 1611.
- [3] A. Vadakkepat, B. Trembacki, S. R. Mathur, J. Y. Murthy, *J. Electrochem. Soc.* **2015**, 163, A119.
- [4] S. C. Chen, C. C. Wan, Y. Y. Wang, *J. Power Sources* **2005**, 140, 111.
- [5] A. Samba, N. Omar, H. Gualous, O. Capron, P. Van den Bossche, J. Van Mierlo, *Electrochim. Acta.* **2014**, 147, 319.
- [6] G. Guo, B. Long, B. Cheng, S. Zhou, P. Xu, B. Cao, *J. Power Sources* **2010**, 195, 2393.
- [7] D. H. Jeon, S. M. Baek, *Energy Convers. Manag.* **2011**, 52, 2973.
- [8] S. F. Schuster, T. Bach, E. Fleder, J. Müller, M. Brand, G. Sextl, A. Jossen, *J. Energy Storage* **2015**, 1, 44.
- [9] P. Ramadass, B. Haran, R. White, B. N. Popov, *J. Power Sources* **2002**, 112, 606.
- [10] P. Ramadass, B. Haran, R. White, B. N. Popov, *J. Power Sources* **2002**, 112, 614.
- [11] G. Zhang, S. Huang, G. J. Nelson, T. Iriyama, G. M. Cavalheiro, *J. Electrochem. Energy Convers. Storage* **2020**, 17, 021101.
- [12] M. Fleckenstein, O. Bohlen, B. Bäker, *World Electr. Veh. J.* **2012**, 5, 322.
- [13] S. Yang, C. Ling, Y. Fan, Y. Yang, X. Tan, H. Dong, *Int. J. Electrochem. Sci.* **2019**, 14, 6077.
- [14] D. Werner, S. Paarmann, A. Wiebelt, T. Wetzel, *Batteries* **2020**, 6, 13.
- [15] D. Werner, S. Paarmann, A. Wiebelt, T. Wetzel, *Batteries* **2020**, 6, 12.
- [16] H. Maleki, S. A. Hallaj, J. Robert Selman, R. B. Dinwiddie, H. Wang, *J. Electrochem. Soc.* **1999**, 146, 947.
- [17] P. Gotcu, W. Pflöging, P. Smyrek, H. J. Seifert, *Phys. Chem. Chem. Phys.* **2017**, 19, 11920.
- [18] F. Richter, S. Kjelstrup, P. J. S. Vie, O. S. Burheim, *J. Power Sources* **2017**, 359, 592.
- [19] A. Loges, S. Herberger, D. Werner, T. Wetzel, *J. Power Sources* **2016**, 325, 104.
- [20] W. J. Parker, R. J. Jenkins, C. P. Butler, G. L. Abbott, *J. Appl. Phys.* **1961**, 32, 1679.
- [21] J. A. Cape, G. W. Lehman, *J. Appl. Phys.* **1963**, 34, 1909.
- [22] R. L. McMasters, J. V. Beck, R. B. Dinwiddie, H. Wang, *J. Heat Transfer* **1999**, 121, 15.
- [23] A. Salazar, A. Sánchez-Lavega, J. Fernández, *J. Appl. Phys.* **1989**, 65, 4150.
- [24] A. Salazar, A. Sánchez-Lavega, J. Fernández, *J. Appl. Phys.* **1991**, 69, 1216.
- [25] M. Bertolotti, R. Li Voti, G. Liakhou, C. Sibilia, *Rev. Sci. Instrum.* **1993**, 64, 1576.
- [26] O. S. Burheim, M. A. Onsrud, J. G. Pharoah, F. Vullum-Bruer, P. J. S. Vie, *J. Electrochem. Soc.* **2014**, 58, 145.
- [27] D. Werner, A. Loges, D. J. Becker, T. Wetzel, *J. Power Sources* **2017**, 364, 72.
- [28] M. Kleiber, R. Joh, in *VDI-Wärmeatlas*, (Eds.: VDI-Gesellschaft), Springer-Verlag, Heidelberg, Germany **2013**, pp. 357–464.
- [29] S. He, B. T. Habte, F. Jiang, *Int. Commun. Heat Mass Transf.* **2017**, 82, 1.
- [30] R. A. Buerschaper, *J. Appl. Phys.* **1944**, 15, 452.
- [31] D. A. G. Bruggeman, *Ann. Phys.* **1935**, 5, 636.
- [32] P. Zehner, E. U. Schlünder, *Chem. Ing. Techn.* **1970**, 14, 933.
- [33] P. Zehner, E. U. Schlünder, *Chem. Ing. Techn.* **1972**, 23, 1303.
- [34] P. Zehner, E. U. Schlünder, *Chem. Ing. Techn.* **1973**, 5, 272.
- [35] E. G. Gilbert, D. W. Johnson, S. S. Keerth, *J. Robot. Autom.* **1988**, 4, 193.
- [36] W. Bauer, D. Nötzel, V. Wenzel, H. Nirschl, *J. Power Sources* **2015**, 288, 359.
- [37] L. Almar, J. Joos, A. Weber, E. Ivers-Tiffée, *J. Power Sources* **2019**, 427, 1.
- [38] L. Pfaffmann, S. Jaiser, M. Müller, P. Scharfer, W. Schabel, W. Bauer, F. Scheiba, H. Ehrenberg, *J. Power Sources* **2017**, 363, 460.
- [39] E. K. Rahani, V. B. Shenoy, *J. Electrochem. Soc.* **2013**, 160, A1153.
- [40] H. Wang, T. Umeno, K. Mizuma, M. Yoshio, *J. Power Sources* **2008**, 175, 886.
- [41] J. Chong, S. Xun, H. Zheng, X. Song, G. Liu, P. Ridgway, J. Q. Wang, V. S. Battaglia, *J. Power Sources* **2011**, 196, 7707.
- [42] S. Lim, S. Kim, K. H. Ahn, S. J. Lee, *J. Power Sources* **2015**, 299, 221.
- [43] M. Indrikova, S. Grunwald, F. Golks, A. Netz, B. Westphal, A. Kwade, *J. Electrochem. Soc.* **2015**, 162, A2021.
- [44] M. Yoo, C. W. Frank, S. Mori, *Chem. Mater.* **2003**, 15, 850-861.
- [45] OpenCFD, OpenFOAM: User Guide, snappyHexMesh, <https://www.openfoam.com/documentation/user-guide/snappyHexMesh.php> (accessed: May 2020).
- [46] P. von Böckh, T. Wetzel, *Wärmeübertragung, Grundlagen und Praxis*, 7th ed., Springer Vieweg, Berlin, Germany **2017**.
- [47] F. Moukalled, L. Mangani, M. Darwish, *The Finite Volume Method in Computational Fluid Dynamics*, Vol. 113, Springer International Publishing, Cham, Switzerland **2016**.
- [48] OpenCFD, OpenFOAM: User Guide, chtMultiRegionFOAM, <https://www.openfoam.com/documentation/guides/latest/doc/guide-applications-solvers-heat-transfer-chtMultiRegionFoam.html> (accessed: May 2020).
- [49] J. C. Maxwell, *A Treatise on Electricity and Magnetism*, Vol. 1, Clarendon Press, Oxford **1873**.
- [50] A. Eucken, *Forschungsarb. Gebiete Ingenieurw.* **1940**, 11, 6.
- [51] R. Landauer, *J. Appl. Phys.* **1952**, 23, 779.
- [52] J. K. Carson, S. J. Lovatt, D. J. Tanner, A. C. Cleland, *In. J. Heat Mass Transf.* **2005**, 48, 2150.
- [53] S. Kirkpatrick, *Rev. Mod. Phys.* **1973**, 45, 574.
- [54] J. Wang, J. K. Carson, M. F. North, D. J. Cleland, *In. J. Heat Mass Transf.* **2006**, 49, 3075.
- [55] E. L. Cussler, *Diffusion: Mass Transfer in Fluid Systems*, 3rd ed., Cambridge University Press, Cambridge, MA **1997**.
- [56] C. Y. Ho, R. W. Powell, P. E. Liley, *J. Phys. Chem. Ref. Data* **1972**, 1, 279.
- [57] K. Takahata, I. Terasaki, *Jpn. J. Appl. Phys.* **2002**, 41, 763.
- [58] J. Cho, M. D. Losego, H. G. Zhang, H. Kim, J. Zuo, I. Petrov, D. G. Cahill, P. V. Braun, *Nat. Commun.* **2014**, 5, 1.
- [59] M. M. Mallick, S. Vitta, *Inorg. Chem.* **2017**, 56, 5827.

- [60] G. Krishna Bama, P. Indra Devi, K. Ramachandran, *J. Mater. Sci.* **2009**, *44*, 1302.
- [61] B. Bonno, J. L. Laporte, R. Tascón d'León, *Meas. Sci. Technol.* **2001**, *12*, 671.
- [62] Quadrant Group, Technical Data Sheet for Polyvinylidene Rod & Sheet-Symalit 1000 PVDF, https://www.theplasticshop.co.uk/plastic_technical_data_sheets/pvdf_technical_data_sheet.pdf. (accessed: May 2020).
- [63] Solvay, Solef PVDF Technical Data Sheets, <https://www.solvay.com/en/brands/solef-pvdf/technical-data-sheets> (accessed: May 2020).
- [64] Reade International Corp., Carbon Black, <https://www.reade.com/products/carbon-black> (accessed: May 2020).
- [65] Y.-J. Kim, Y.-F. Tan, S. Kim, *J. Compos. Mater.* **2017**, *52*, 2047.
- [66] T. N. G. Adams, T. R. Olson, J. A. King, J. M. Keith, *Polym. Compos.* **2011**, *32*, 147.
- [67] R. L. Hamilton, O. K. Crosser, *Ind. Eng. Chem. Fundam.* **1962**, *1*, 187.
- [68] Y. He, H. T. Li, L. X. Ma, *Adv. Mater. Res.* **2009**, *87–88*, 86.
- [69] J. K. Oleiwi, M. S. Hamza, N. A. Nassir, *Eng. Tech. J.* **2011**, *29*, 856.
- [70] R. Ram, V. Soni, D. Khastgir, *Compos. B Eng.* **2020**, *185*, 1.
- [71] M. Ender, *J. Power Sources* **2015**, *282*, 572.